Structural Durability & Health Monitoring

Tech Science Press

https://doi.org/10.32604/sdhm.2026.079382

ARTICLE

Quantitative Delamination Imaging in CFRP Composites Using Lamb Waves: Accounting for Material Uncertainty via the FBP Method

Kai Luo[1,2,*] **and Yuzhi Chen**[3]

[1]Shenzhen Key Laboratory of Intelligent Manufacturing for Continuous Carbon Fibre Reinforced Composites, Southern University of Science and Technology, Shenzhen, China
[2]School of Automation and Intelligent Manufacturing (AIM), Southern University of Science and Technology, Shenzhen, China
[3]Faculty of Civil Engineering, Brno University of Technology, Brno, Czech Republic

*Corresponding Author: Kai Luo. Email: luokai@alu.uestc.edu.cn

Received: 20 January 2026; Accepted: 28 April 2026; Published: 24 August 2026

ABSTRACT: Material property variability in carbon fiber-reinforced polymer composites is a major source of uncertainty in quantitative Lamb wave-based delamination imaging. Even minor deviations in elastic properties can alter dispersion characteristics and wave propagation behavior, thereby reducing the reliability of imaging-based assessments. To systematically investigate this effect, the present study examines the influence of subtle material variations on Lamb wave responses through combined numerical modeling and finite element simulations. Time-of-flight features at the excitation frequency are extracted using a continuous wavelet transform with Morlet wavelets, enabling robust identification of mode-dependent arrival information. Within a finite element framework, A_0 mode propagation in the presence of delamination is simulated, and damage imaging is subsequently carried out using a filtered back-projection algorithm. To improve boundary definition and support quantitative characterization, morphological filtering is combined with Canny edge detection to refine the reconstructed damage contours. The results show that the proposed filtered back-projection-based imaging framework provides clear and accurate visualization of delamination while exhibiting reduced sensitivity to material property uncertainty. Delaminations with different geometric characteristics are consistently identified, demonstrating enhanced robustness against material variability. These findings confirm the effectiveness of the proposed Lamb wave-based approach for reliable, quantitative delamination imaging in composite structures.

KEYWORDS: Ultrasonics; Lamb wave; guided waves; damage detection; damage imaging; finite element (FE); material uncertainty; carbon fiber-reinforced polymer (CFRP)

1 Introduction

Carbon fiber-reinforced polymer (CFRP) composite panels are widely used in aerospace, infrastructure, and transportation engineering due to their high specific strength and stiffness, low density, and excellent corrosion and fatigue resistance [1–4]. These attributes make CFRP laminates particularly suitable for primary load-bearing structural components.

Despite these advantages, CFRP structures are susceptible to progressive damage accumulation over the long term, which can seriously compromise structural safety and reliability if not detected in a timely manner. In engineering applications such as aircraft, wind turbine blades, and ground vehicles, cyclic loading commonly induces multiple damage modes, including matrix cracking, fiber fracture, delamination, and manufacturing-related defects [5–7]. Damage typically initiates with matrix cracking and fiber breakage, whereas delamination plays a dominant role in stiffness degradation and often governs the transition toward catastrophic failure under increasing load levels [8]. Because delamination is usually subsurface, its reliable detection remains a significant challenge, underscoring the need for effective structural health monitoring techniques for composite structures.

Conventional inspection and monitoring methods often suffer from limited accuracy, long inspection durations, and strong dependence on baseline signals acquired from pristine structures, which restricts their applicability in practical engineering environments [9–12]. Ultrasonic Lamb wave-based non-destructive testing techniques have therefore attracted increasing attention for composite inspection and monitoring [13,14]. Their advantages include long propagation distances, high sensitivity to various types of damage, ease of implementation, and non-destructive operation. Structural damage modifies local stiffness, mass distribution, and strain energy, thereby perturbing Lamb wave dispersion and propagation behavior. These perturbations manifest as measurable changes in wave velocity, phase, and time of flight, providing the physical basis for Lamb-wave-based damage detection [15].

Most existing Lamb wave-based evaluation methods extract damage information by comparing signals recorded by distributed transducers, often relying on reference measurements obtained from an undamaged state [16,17]. Representative approaches include time-of-flight-based elliptical localization for crack detection [18], baseline-dependent piezoelectric response analysis for structural monitoring [19], and data-driven damage imaging methods based on convolutional neural networks [20]. Although effective in many cases, these approaches remain limited by baseline dependence and reduced robustness, particularly when accurate characterization of delamination location, size, and geometry is required [21,22].

Finite element modeling has become an indispensable tool for simulating Lamb wave propagation in plate-like structures, providing accurate representations of mechanical and acoustic behavior with good agreement with experimental observations [13,23]. In addition, numerical modeling enables systematic investigation of material property variations that are difficult to isolate experimentally, making it well-suited for studying the influence of material uncertainty on Lamb wave dispersion and propagation characteristics.

Within this context, the present study develops a Lamb wave-based damage imaging framework that integrates multi-probe sensing with a filtered back-projection (FBP) algorithm. FBP reconstructs damage images from projection data collected by equidistantly distributed sensors and is widely used in tomographic imaging because of its computational efficiency and conceptual simplicity [24,25]. The method is based on the Fourier central slicing theorem, which relates one-dimensional projection data to the two-dimensional spatial distribution of structural features [26].

Accurately quantifying the influence of material property uncertainty on damage reconstruction remains challenging, especially for complex delamination geometries such as elliptical defects. Even relatively small deviations in material properties, typically on the order of five to ten percent, can significantly alter Lamb wave dispersion behavior and time of flight measurements, leading to degraded reconstruction accuracy. To date, limited effort has been devoted to systematically examining how such subtle material variations affect dispersion characteristics and wave transmission behavior.

To address this limitation, a comprehensive investigation of Lamb wave propagation in CFRP composite plates is conducted using a combination of analytical modeling and finite element simulation. The effects of material property deviations on dispersion curves and wave propagation behavior are systematically analyzed and compared. Time-of-flight (TOF) information is extracted from simulated responses using a continuous wavelet transform and subsequently used as projection data for FBP imaging. In the numerical model, an elliptical delamination is introduced using a volume segmentation approach, and a simplified global perturbation of eight percent is introduced into the elastic properties for controlled numerical sensitivity analysis.

To improve computational efficiency while maintaining accuracy, piezoelectric transducers are modeled using a point force approximation. The results show that delaminated regions amplify non-linear variations in TOF along sensing paths, and that the proposed imaging and quantification framework effectively mitigates the influence of material uncertainty through dual-scale morphological filtering (DSMF) combined with Canny edge detection. These findings confirm the capability of the proposed approach to reliably reconstruct delamination and quantitatively characterize CFRP composites under material uncertainty.

2 Basic Theoretical Background

To ensure uniform spatial sampling of Lamb wave propagation paths, damage imaging based on the filtered back-projection method is implemented using a fan-beam sensor array configuration. In this framework, projection data acquired at different angular positions are first convolved before back projection. This preprocessing step suppresses shape-related artifacts associated with the point spread function and improves the fidelity of the reconstructed damage images.

The TOF of the ultrasonic Lamb wave in the composite plate is substituted into the FBP reconstruction algorithm as the projection value $T_{\beta i}(n\alpha)$ of the path where each pair of transducers is located. Specifically, the TOF is defined as the time difference between the peak of the first A_0 mode wave packet in the received signal and the peak of the excitation wave packet. During the reconstruction process, TOF data collected from detector pairs distributed at equal angular intervals within the fan beam sector are transformed into the frequency domain using a one-dimensional Fourier transform. The transformed data are then filtered using a predefined filter function to obtain direction-dependent projection information. Finally, inverse projection is performed in all directions, and the resulting values are uniformly assigned to the corresponding pixels along the original propagation paths, producing the final FBP-reconstructed image.

Rather than identifying local peaks based on signal envelopes, the TOF is estimated using the time location corresponding to the maximum local wave energy measured by each PZT sensor. Complex Morlet wavelets are adopted for this purpose because they enable effective separation of amplitude and phase information in Lamb wave signals and provide localized characterization of instantaneous frequency and temporal evolution.

Furthermore, a revised TOF-based reconstruction strategy is adopted to account for the influence of material anisotropy in composite laminates on wave propagation characteristics, thereby improving the accuracy of TOF estimation and damage imaging [26–29]. Since CWT has an excellent resolution in the time and frequency domains, Yan [27] redefines the signal of the Lamb waveform by using two parameters, a and b, where a and b are used to scale and translate the mother wavelet function $\psi(t)$, respectively. The CWT of a l wave signal $L_s(t)$ can be defined as

$$CWT(a,b) = \frac{1}{\sqrt{a}} \int_{-\infty}^{\infty} L_s(t)\, \psi^* \left(\frac{t-b}{a}\right) \mathrm{d}t \tag{1}$$

where a and b denote the scale and translation parameters, respectively, and * denotes complex conjugation. The corresponding kernel function is

$$\psi_{(a,b)}(t) = \frac{1}{\sqrt{a}} \psi\left(\frac{t-b}{a}\right) \tag{2}$$

In the present study, a complex Morlet wavelet is adopted to analyze the dispersive Lamb wave signal. The mother wavelet is expressed as:

$$\psi_{(a,b)}(t) = \frac{1}{\sqrt{a}} \psi\left(\frac{t-b}{a}\right) \tag{3}$$

where f_c and f_b are the center-frequency and bandwidth parameters, respectively. For the adopted wavelet, $f_c = f_b = 1$.

For the CWT representation, the local energy concentration is characterized by the squared modulus of the wavelet coefficients, namely the scalogram

$$|CWT(a,b)|^2 = CWT(a,b)\,CWT^*(a,b) \tag{4}$$

The pseudo-frequency corresponding to scale a is related to the sampling frequency f_s, by

$$f = \frac{f_c}{a} f_s \tag{5}$$

In the present study, the CWT analysis is performed at the scale corresponding to the excitation center frequency of 200 kHz, where the scale is determined from the scale-frequency relationship $f = (f_c/a)\,f_s$. For the adopted complex Morlet wavelet with $f_c = 1$, the corresponding scale is $a_{200} = f_s/200$.

The upper part of Fig. 1 shows a typical Lamb wave signal, and the lower figure shows its energy-time plot obtained after the proposed CWT transform.

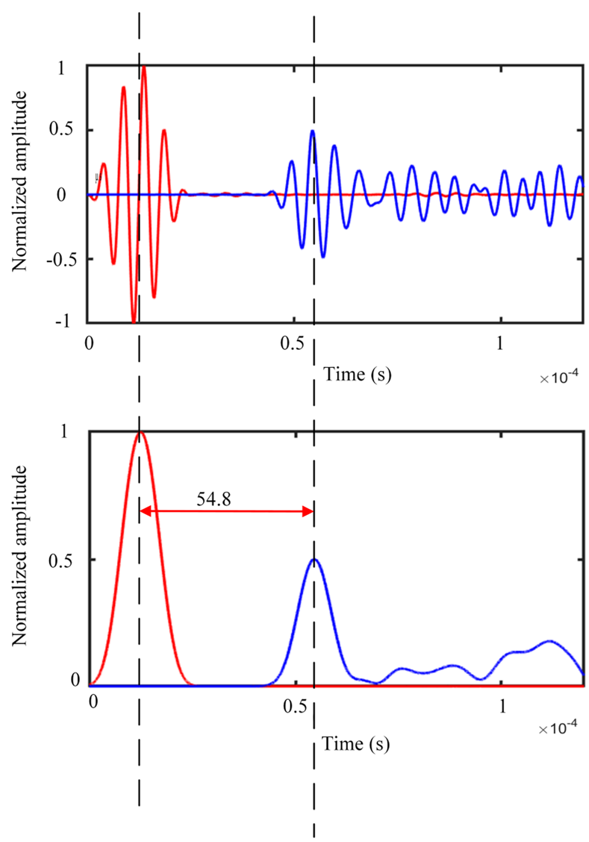

Figure 1: Schematic diagram of CWT-based Lamb wave TOF calculation.

Fig. 1 shows that the maximum of the energy envelope obtained from the continuous wavelet transform does not exactly coincide with the peak of the time domain waveform. This difference arises from the narrowband tone burst excitation used in the experiments. Although most of the signal energy packet is concentrated near the center frequency, spectral leakage into neighboring frequency components is unavoidable. As a result, the energy envelope derived from the CWT reflects the energy distribution associated with the instantaneous frequency content at the selected scale rather than the absolute amplitude peak of the raw time domain signal. In the present study, the TOF definition is based on the time interval corresponding to the directly propagated wave packet, rather than on the full signal window containing later reflected components.

The time location at which the CWT energy is most concentrated is therefore considered a more reliable indicator of wave arrival. By using this energy concentration point to define the time of flight, the estimation error introduced by directly subtracting peak locations from the original excitation signal and the received direct wave is effectively reduced. As a result, more accurate TOF values are obtained by computing the time difference between the excitation peak and the peak of the CWT-based energy associated with the direct wave.

The revised TOF data are subsequently incorporated into the filtered back projection reconstruction algorithm as projection values, enabling reliable damage imaging of the composite plate.

To reduce the risk of misidentifying a scattered wave packet as the direct A0 mode arrival under strong scattering, multipath propagation, and boundary reflection conditions, the TOF in this study is not determined solely by the maximum CWT amplitude peak, but is identified with reference to the expected arrival time window constrained by the sensing path geometry and the scale range corresponding to the dominant energy of the A_0 mode.

It should be noted that the present method does not rely on experimentally measured healthy baseline signals, whereas its TOF estimation and image reconstruction still depend on the underlying guided wave propagation assumptions and the associated parameter settings.

The detectors are equidistantly distributed on a circular arc centered at O. S represents the detector currently exciting the Lamb wave, β is the angle between S and the x and y-axes, and γ is the angle of the sector beam through the point $P(x, y)$, as shown in Fig. 2.

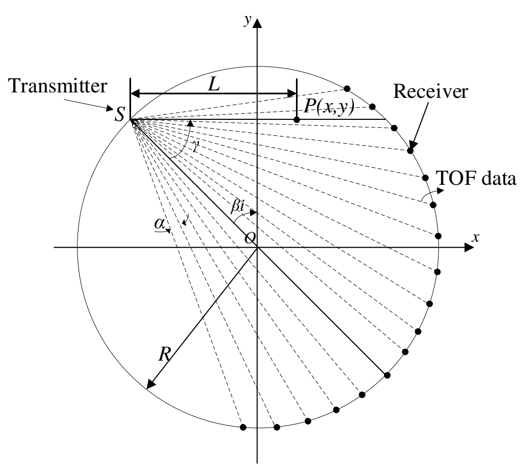

Figure 2: Schematic diagram of the geometric description of the FBP reconstruction technique.

βi is the ith angle of the projection, and the convolution filtering is performed on the projection data; the filtered projection $Q_{\beta i}(n\alpha)$ is known by convolving each modified projection $T_{\beta i}^{m}(n\alpha) = T_{\beta i}(n\alpha) \cdot R \cdot \cos(n\alpha)$ with $g(n\gamma)$:

$$Q_{\beta i} = \left[T_{\beta i}(n\alpha) \cdot R \cdot \cos(n\alpha)\right] * g(n\alpha) \tag{6}$$

where $g(n\gamma)$ is a high pass filter response:

$$g(n\alpha)=\begin{cases}\dfrac{1}{8\alpha^2}, n=0\\ 0, n\ \ is\ \ even\\ \left(-\dfrac{1}{2\pi^2\sin^2 n\alpha}\right), n\ \ is\ \ odd\end{cases} \tag{7}$$

The tomographic image $f(x,y)$ reconstructed by the equirectangular sector FBP algorithm can be described as [21–24]:

$$f(x,y)\approx\frac{2\pi}{N}\sum\nolimits_{i=1}^{N}\frac{Q_{\beta i}(\gamma')}{L^2(x,y,\beta i)} \tag{8}$$

where N is the number of sensors and L is the distance from the actuator to the point $P(x,y)$. $Q_{\beta i}(\gamma')$ is an interpolation of $Q_{\beta i}(\gamma)$. The interpolation method is used to calculate $Q_{\beta i}(\gamma)$. To improve the image quality, it is recommended to enhance the image with cubic spline interpolation [23].

Ultrasonic images reconstructed using the filtered back projection technique are often contaminated by noise and reconstruction artifacts. To address this issue, Luo et al. [23] introduced a multi-scale morphological filtering strategy employing structural elements of different sizes, which effectively suppresses noise while preserving the geometric integrity of damage boundaries. $f(x,y)$ is the ultrasonic reconstruction image and $g(x,y)$ is the structural element. D_f and D_g are the definition domains of $f(x,y)$ and $g(x,y)$. Define the gray-level dilation operator, gray-level erosion operator, opening operation, and closing operation as:

$$f\oplus g=\max\left\{(f(s-x,t-y)+g(x,y)\,\middle|\,(s-x,t-y)\in D_f;(x,y)\in D_g\right\} \tag{9}$$

$$f\ \Theta\ g=\min\left\{(f(s+x,t+y)-g(x,y)\,\middle|\,(s+x,t+y)\in D_f;(x,y)\in D_g\right\} \tag{10}$$

$$(f\circ g)=(f\ \Theta\ g)\oplus g \tag{11}$$

$$(f\cdot g)=(f\oplus g)\,\Theta\ g \tag{12}$$

In morphological image processing, dilation replaces the pixel value within a local neighborhood with the maximum value, whereas erosion assigns the minimum value within the neighborhood. The opening operation, defined as erosion followed by dilation, is used to suppress small bright features and protrusions. In contrast, the closing operation, defined as dilation followed by erosion, removes dark details, fills pores, and bridges narrow gaps or cracks in the image.

Using a single structural element scale, however, often results in limited noise suppression and insufficient preservation of fine edge details. To overcome this limitation, a DSMF strategy is adopted, in which structural elements of two different sizes are alternately applied to the FBP reconstructed ultrasonic images. In these images, the background is mainly gray to black, whereas reconstruction artifacts generally appear as bright regions. Large scale structural elements provide stronger noise suppression, while small scale structural elements are more effective in preserving damage boundary details. By combining these complementary effects, the proposed DSMF approach enhances noise reduction while maintaining boundary integrity. Accordingly, the single direction DSMF operator for image processing can be expressed as follows:

$$Q_i(f)=[((f\cdot g_1)\circ g_1)\cdot g_3]\oplus g_{2i}-[((f\cdot g_1)\circ g_3)]\,\Theta g_2 \tag{13}$$

Using uniform weights $\omega_i=\frac{1}{4}$ to ensure the continuity of the image in all directions, the morphological DSMF structure operator of the FBP image can be expressed as:

$$Q(f) = \sum_{i=1}^{4} \omega_i Q_i(f) \tag{14}$$

3 Experiment and FE Simulation Based on the Point Force Method

Previous studies have experimentally validated the effectiveness of the filtered back projection method and demonstrated the reliability and accuracy of finite element simulations for guided wave analysis [23]. Building on these established results, the present work systematically examines the influence of material property variations on guided wave transmission characteristics, including wave velocity, wavelength, and overall propagation behavior.

In particular, this study evaluates whether damage quantification strategies for composite structures based on FBP and dual scale morphological filtering remain applicable and robust in the presence of material property uncertainty. To further verify the numerical modeling results, the A_0 mode phase velocity obtained from finite element simulations [30] using the point force excitation approach is compared with predictions from the Dispersion Calculator v2.4 Lamb wave frequency dispersion software developed by Imperial College of Science and Technology [31]. The comparison shows good overall agreement between the two approaches, confirming the consistency and reliability of the numerical simulations and dispersion analysis.

3.1 FE Simulation Based on the Point Force Method

To evaluate the adaptability of ultrasonic Lamb wave-based FBP imaging to material uncertainty in composite laminates and to assess its feasibility for damage diagnosis, numerical simulations were conducted using the finite element software ABAQUS. Theoretical analysis and three-dimensional finite element modeling of a T300/7901 composite plate were performed within the ABAQUS/Explicit simulation environment [30]. The material properties of the T300/7901 composite employed in the simulations are summarized in Table 1. To accurately represent the composite plate behavior, the C3D8R reduced-integration solid element was used throughout the numerical model. Quasi-isotropic Uni Tape $[45°/-45°/0°/90°]_{2S}$ was used for lay-up. The CFRP composite plate was laid up by the alternating method with each layer thickness of 0.125 mm, a total of 16 layers, and the total thickness of the plate was 2 mm.

Table 1: Material properties of the T300/7901 composite plate.

Material Properties	$\rho\ (\mathrm{kg/m^3})$	E_1 (GPa)	E_2 (GPa)	G_{12} (GPa)	v_{12}	v_{23}
Value	1560	135	10.9	4.7	0.285	0.4

Note: ρ = density; E = Young's modulus; ν = Poisson's ratio; G = shear modulus.

Lamb wave propagation in plate structures is inherently complex due to its multimodal and dispersive characteristics, which often leads to complicated received signals. For practical non-destructive testing applications, it is therefore desirable to isolate and utilize a single dominant mode. Among the available modes, the fundamental antisymmetric A_0 mode is particularly attractive owing to its strong sensitivity to various damage types, long propagation range, and ease of excitation.

In the present simulations, the point force method is adopted in place of conventional piezoelectric transducer modeling to reduce modeling complexity and computational cost while maintaining sufficient accuracy [32–35]. This approach enables efficient excitation of the A_0 mode without explicitly modeling the electromechanical coupling of PZT sensors [36,37].

The Lamb wave excitation source is simulated using a point-force representation of a PZT. The feasibility and accuracy of this method for modeling Lamb wave generation by PZT transducers have been thoroughly described and validated by Nieuwenhuis et al. [32], demonstrating that the point force approximation can reliably capture transducer behavior with significantly reduced model complexity. In this framework, the excitation signal is introduced into the composite plate through out-of-plane forces applied normal to the surface, thereby preferentially exciting the pure A_0 mode. The effect of the PZT electric field on wave generation is thus approximated by an equivalent mechanical force acting on the plate.

In contrast to traditional modeling approaches that require explicit representation of the PZT geometry, material properties, and electrical coupling, the point force method offers a simplified yet accurate alternative. As illustrated in Fig. 3a, full PZT modeling involves complex sensor–structure interactions, whereas the point-force configuration shown schematically in Fig. 3b approximates the dominant effects of the PZT sensor using two concentrated forces. In this model, the sensor diameter is denoted by a, and the plate thickness is denoted by h. The PZT-force receiver uses the point corresponding to the upper surface as a model by monitoring the stress σ_{13} at that point as the received signal.

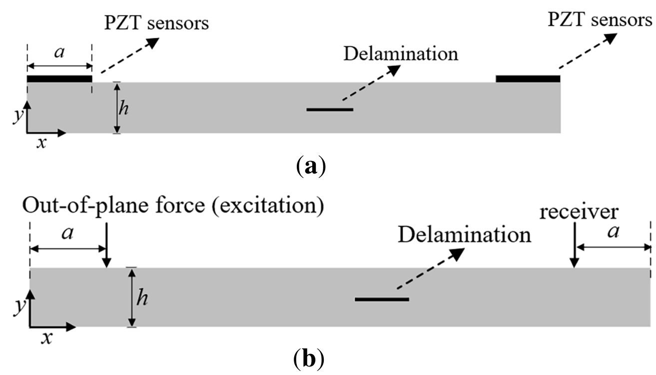

Figure 3: Schematic diagram of the point force method (**a**) Geometric simulation of conventional boards and PZT sensor setup. (**b**) PZT-point force model for FE simulations.

The out-of-plane force at this point is monitored as the received signal. The output uses the out-of-plane force as the output stress, with the direction of the out-of-plane force perpendicular to the specimen to obtain a pure Lamb wave A_0 mode waveform.

To introduce an idealized delamination like discontinuity for imaging oriented numerical assessment, a volume partitioning technique is employed to construct delamination geometries within the composite plate. This approach allows both circular and elliptical delamination configurations to be generated. In the present study, a more complex elliptical delamination is explicitly considered in order to better reflect realistic damage scenarios. It should be noted that this idealized representation is introduced for imaging-oriented numerical assessment only, and does not account for interfacial mechanisms such as cohesive traction separation, contact interaction, or kissing-bond behavior.

A total of 64 sensors are uniformly distributed at equal angular intervals along a circular array with a radius of 40 mm, as shown in Fig. 4 [23]. To reduce the influence of boundary reflections on the inspection region and to ensure that direct wave propagation paths remain unaffected, a protective buffer zone with a width of 40 mm is introduced around the perimeter of the detection area. This configuration effectively isolates the region of interest from reflected wave interference during signal acquisition.

Previous studies have confirmed the reliability and accuracy of ultrasonic Lamb wave-based filtered back projection imaging for circular damage characterization [21–23]. In the current configuration, the sensor array is defined so that the first sensor is positioned at a prescribed angular reference location, with the remaining sensors distributed uniformly clockwise at equal angular intervals.

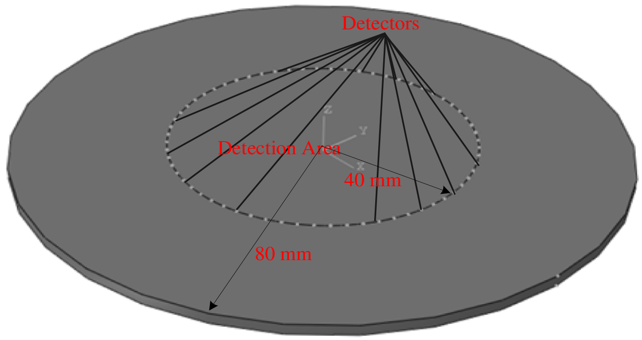

Figure 4: Schematic diagram of circular plate grid setup and sensor position setup.

Delamination damage is modeled at the center of the composite plate using a volume partitioning technique [38]. The finite element mesh employs elements with dimensions of 0.5 mm × 0.5 mm × 0.125 mm along the in-plane and thickness directions, respectively. As illustrated in Fig. 4, 64 PZT sensors are arranged in a circular configuration along the boundary of the detection region and implemented using the point-force modeling approach.

The total solution time was 120 μs with a step size of 40 μs using ABAQUS/explicit dynamic analysis. An elliptical damage located at a skewed position with long and short semi-axes of 4 and 3 mm, respectively, was set. The delamination defects were located in the seventh and eighth layers of the composite plate, each with a thickness of 0.25 mm. The locations of the defects are shown in Fig. 5.

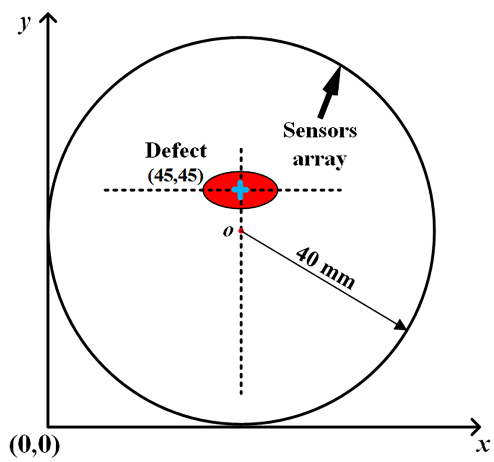

Figure 5: The actual composite plate detection area and elliptical defect location diagram.

Numerical simulation of Lamb wave propagation inherently involves modal decomposition and dispersion curve analysis. In practice, dispersion characteristics are commonly obtained using analytical or semi analytical approaches, each associated with different levels of implementation complexity and inherent limitations. Dispersion curves provide essential insight into guided wave behavior, including phase and group velocities, wavenumber evolution, cutoff frequencies, modal relationships, energy distribution, and waveform variation with propagation distance.

For composite plates, modal decomposition and dispersion tracking are particularly challenging because of the anisotropic nature of individual plies, even when the laminate is designed to be quasi-isotropic through stacking sequence optimization. As a result, the coupling and decoupling behavior of guided wave modes is governed by the laminate stiffness matrix formulation. In the present analysis, horizontal shear wave components are neglected due to their minimal contribution under low frequency excitation and thin-plate conditions. This simplification allows the investigation to focus exclusively on the fundamental antisymmetric A_0 Lamb wave mode.

The relationships between material properties and key wave characteristics, including wave velocity, dispersion behavior, and amplitude attenuation, are derived using stiffness matrix-based modeling. The theoretical formulation and dispersion analysis follow established algorithms developed by Huber and Liu et al. [39,40], and other related dispersion-modeling studies [41,42], which provide a robust and widely accepted framework for Lamb wave analysis in anisotropic composite laminates.

3.2 Validation of Mode Selection and Finite Element Simulation Results

The product of the Lamb wave center frequency and the composite plate thickness directly determines the number of propagating Lamb wave modes. The group velocity waveforms of Lamb wave A_0 and S_0 modes were plotted using Dispersion Calculator v2.4 for the 16-layer T300/7901 composite laminate simulation analysis, shown in Fig. 6.

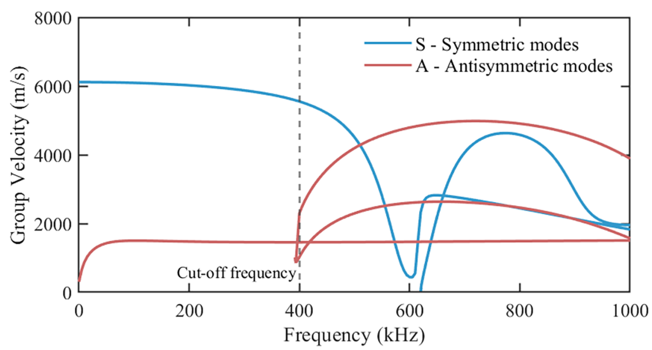

Figure 6: Dispersion in 2 mm T300/7901 Quasi-isotropic Uni Tape $[45°/-45°/0°/90°]_{2S}$.

As can be seen from Fig. 6, the higher order modes of Lamb waves cut off at 400 kHz, and the relatively low frequency of excitation can effectively reduce the mode spurious and dispersion. The Lamb wave thickness-displacement diagrams for the different modes are given in Fig. 7.

As indicated by the thickness–displacement profiles shown in Fig. 7, when an excitation frequency of 200 kHz is selected, the out-of-plane displacement amplitude of the A_0 mode is substantially higher than that of the S_0 mode. Under vertical excitation implemented through the point-force approach in the finite element model, a predominantly pure A_0 Lamb wave can therefore be generated when only the out-of-plane displacement component is considered, while the contribution of the S_0 mode becomes negligible.

The A_0 mode is characterized by pronounced out-of-plane displacement, making it particularly suitable for vertical excitation and reception schemes. Although its in-plane displacement component is smaller than that of the S_0 mode, the A_0 mode exhibits significantly higher out-of-plane displacement energy, which is essential for effective signal reception. Accordingly, a direct vertical excitation configuration at 200 kHz is adopted in this study to excite the A_0 mode preferentially and to minimize interference from mode conversion and multimodal mixing. In addition, the A_0 mode demonstrates strong sensitivity to various damage types and possesses adequate penetration capability, rendering it more readily excitable and more practical for engineering applications compared with the S_0 mode.

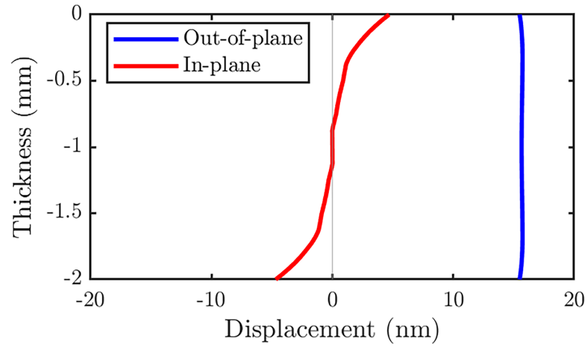

(**a**)

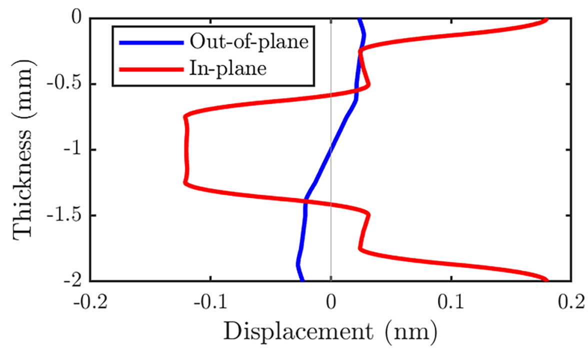

(**b**)

Figure 7: Schematic diagram of Lamb wave thickness-displacement, (**a**) A_0 mode, (**b**) S_0 mode.

It should be emphasized that even minor variations in material properties can induce non-linear modifications in Lamb wave dispersion characteristics. Although such changes may appear subtle at the dispersion curve level, their effects accumulate with increasing propagation distance, leading to noticeable variations in time of flight, signal amplitude, and waveform morphology. These accumulated discrepancies can introduce relative errors in subsequent signal processing and imaging procedures, thereby increasing the likelihood of imaging artifacts and false indications.

It should be noted that the macroscopic mechanical properties of composite materials are inevitably influenced by manufacturing processes, batch variations, and fluctuations in fiber volume fraction. Even for nominally identical material systems, their elastic properties may exhibit a certain degree of variability. Previous studies have shown that such uncertainties are primarily manifested as variations between different specimens or batches, while within a single structural component, the material properties can generally be approximated as spatially uniform, leading to a globally consistent mechanical response at the macroscopic scale.

Based on this understanding, the variation of material properties in the present numerical modeling is treated as a global and uniform perturbation, where elastic parameters are assumed to vary consistently throughout the structure rather than locally. Within this framework, the individual effects of key parameters, including E_1, E_2 and G_{12}. In the present work, a representative deviation level of 8% is introduced to the selected material parameters to evaluate the robustness of the proposed imaging framework under a relatively conservative uncertainty condition [43,44]. This perturbation is applied simultaneously to the laminate elastic parameters, representing a global variation of the effective material properties. Such a setting aims to emulate realistic manufacturing-induced variability at the structural scale.

To further illustrate the influence of such property variations on Lamb wave propagation, the dispersion curves of group velocity, wavelength, and wavenumber as functions of frequency are presented in Figs. 8–10, where the baseline case is compared with the corresponding 8% deviation case.

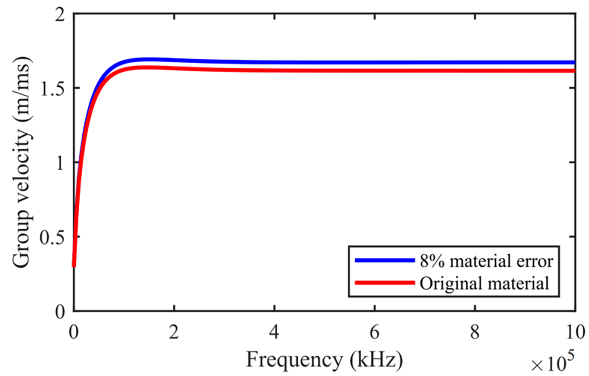

Figure 8: Schematic diagram of Lamb wave time-frequency curves with different material properties (A_0 mode).

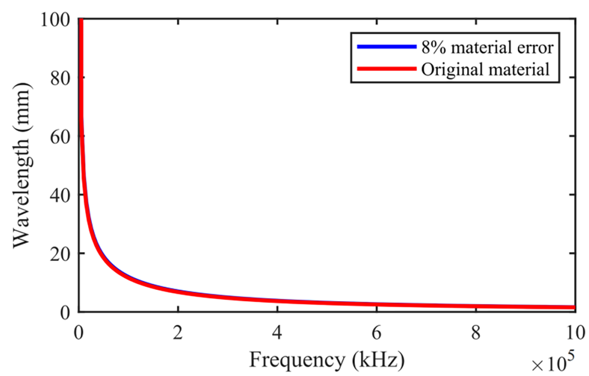

Figure 9: Schematic diagram of Lamb wave time-wavelength curves with different material properties (A_0 mode).

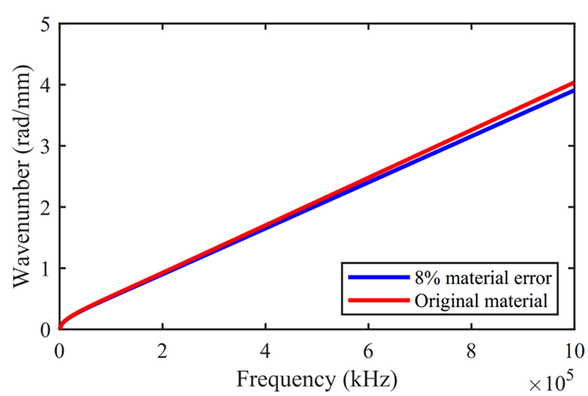

Figure 10: Schematic diagram of Lamb wave time-wavenumber curves with different material properties.

As shown in Figs. 8–10, variations in material properties do not affect the dispersion characteristics of Lamb waves in a uniform manner. Instead, different wave parameters exhibit distinct sensitivities to material uncertainty. For the A_0 mode, an increase in material stiffness results in a noticeable rise in wave velocity.

Specifically, the peak group velocity increases from 1637.5 to 1691.7 m/s, corresponding to a 3.31% increase. At the excitation frequency of 200 kHz, the phase velocity increases from 1631.9 to 1686.8 m/s, representing a comparable variation of 3.36%.

Correspondingly, the wavelength shows a moderate increase, while the wavenumber decreases. At 200 kHz, the wavelength increases from 6.79 to 6.98 mm, corresponding to a relative variation of approximately 2.8%, whereas the wavenumber exhibits a reduction of approximately 4.6%. These results indicate that even moderate material deviations can induce measurable changes in wave propagation characteristics.

To further interpret the physical influence of individual material parameters on guided wave propagation, additional sensitivity analyses are conducted by varying key elastic constants, including E_1, E_2 and G_{12}, independently, as shown in Figs. 11–13. In particular, variations in E_2 and G_{12}, are more strongly influenced by matrix-related mechanical characteristics, induce significantly stronger changes in both phase velocity and group velocity of the A_0 mode, especially in the low-frequency regime. In contrast, variations in E_1 show a comparatively weaker influence on the A_0 mode, while their effect becomes relatively more noticeable in the higher-frequency range and on the S_0 mode.

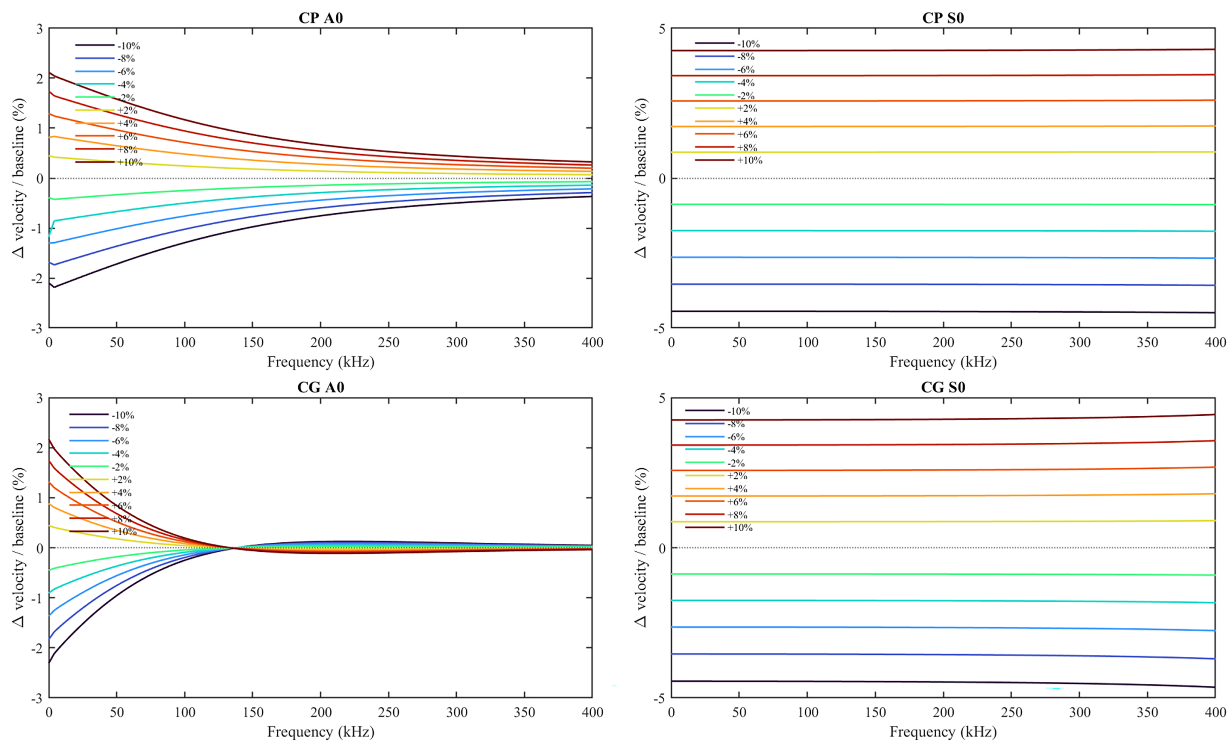

Figure 11: Effect of longitudinal Young's modulus E_1 variation on the phase and group velocities of guided waves.

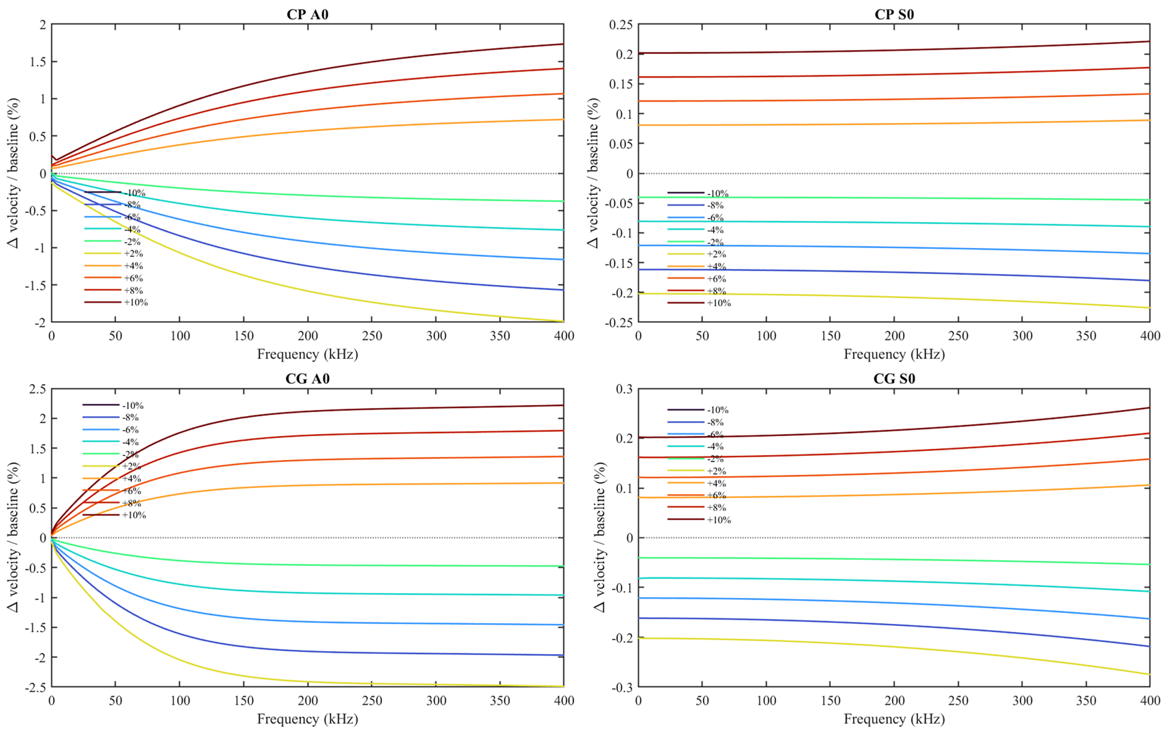

Figure 12: Effect of transverse Young's modulus E_2 variation on the phase and group velocities of guided waves.

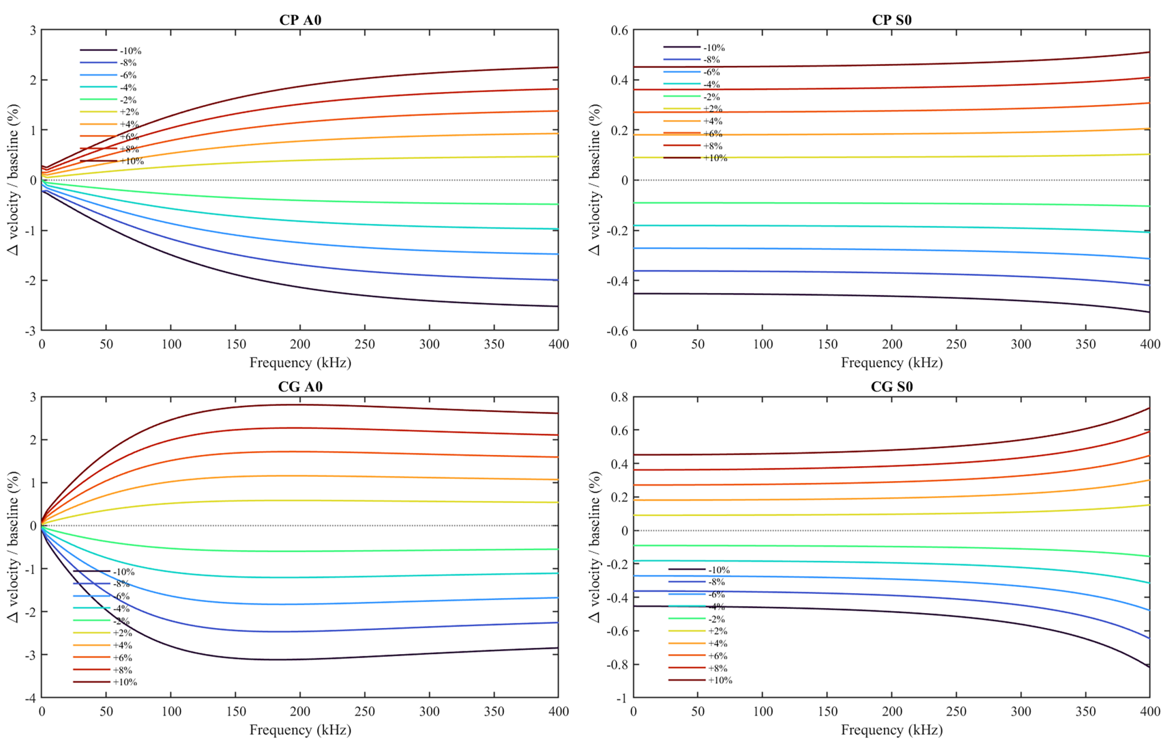

Figure 13: Effect of in-plane shear modulus G_{12} variation on the phase and group velocities of guided waves.

This observation is consistent with the physical nature of Lamb wave propagation in composite laminates, where the A_0 mode is more sensitive to transverse and shear stiffness components. Therefore, the uncertainty associated with matrix-dominated properties plays a dominant role in influencing guided wave behavior.

It should be emphasized that the global perturbation and individual parameter variation analyses serve different purposes. The global perturbation is employed to simulate realistic manufacturing-induced uncertainty at the structural level, while the individual parameter variations are introduced to provide physical insight into the relative contributions of different elastic constants.

These results demonstrate that material property variations induce non-uniform modifications in Lamb wave dispersion behavior. Although the variations in velocity may appear moderate, their effects accumulate over propagation distance, leading to noticeable deviations in time of flight, signal amplitude, and waveform morphology. Since the FBP imaging framework relies on time-of-flight information as the projection parameter, such variations can significantly degrade imaging accuracy and compromise quantitative damage characterization if material uncertainty is not properly considered.

4 Results and Discussion

Previous studies have demonstrated that FBP based imaging can be effectively applied to homogeneous plates with different material properties, including composite laminates with varying parameters as well as metallic plates, without requiring prior knowledge of the material type [23,24,28]. These results confirm the broad applicability of the FBP method across a wide range of structural materials.

In practical engineering applications, however, material properties are inevitably affected by manufacturing variability, processing conditions, transportation, and service environments. These factors introduce spatially non uniform material uncertainty, which leads to discrepancies between numerical simulations and experimental measurements and, more importantly, poses a significant challenge to the robustness of damage imaging and recognition algorithms.

Based on finite element simulation data, the present study systematically investigates the influence of material property variations on the performance of FBP based imaging. Damage reconstruction results obtained using nominal material parameters are presented in Fig. 14. In addition, the effect of material uncertainty on imaging accuracy and damage identification is evaluated by introducing an eight percent deviation in the material properties of the T300/7901 composite laminate. This analysis provides a quantitative assessment of the robustness of the proposed imaging framework under realistic material uncertainty conditions.

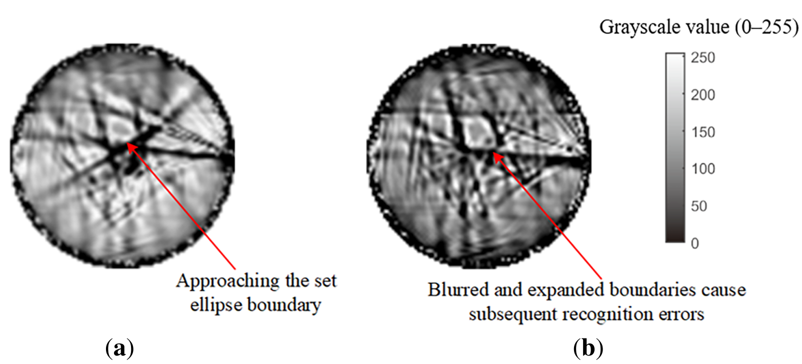

Figure 14: Comparison of imaging differences due to material uncertainty: (**a**) Original material parameters FBP imaging, (**b**) 8% material error parameters FBP imaging.

Fig. 14a presents the FBP reconstructed damage image obtained using the nominal T300/7901 material parameters. When an 8% deviation is introduced into the material properties, as shown in Fig. 14b, the reconstructed damage image exhibits noticeable but limited differences from the nominal-parameter result. In particular, the reconstructed damage boundaries become rougher and less well defined, accompanied by increased blurring and a higher level of reconstruction artifacts surrounding the damage region.

These effects are mainly attributed to errors in TOF estimation caused by material property uncertainty, which are further intensified by the anisotropic characteristics of composite laminates. As a result, the reconstructed damage region slightly exceeds the actual delamination boundary, leading to an overestimation of the damage extent. This boundary expansion directly reduces the accuracy of subsequent damage identification and edge detection processes.

Despite the local degradation in boundary quality, the overall location and global shape of the reconstructed damage remain in good agreement with the elliptical delamination geometry shown in Fig. 4. This observation indicates that the proposed FBP based imaging framework maintains stable performance under material property uncertainty and demonstrates a degree of robustness against interference effects. The results further confirm the applicability of the proposed approach to composite plates with varying material properties.

Fig. 15 illustrates the change in Lamb waveform for the same sensing path with the wrong original material and material properties.

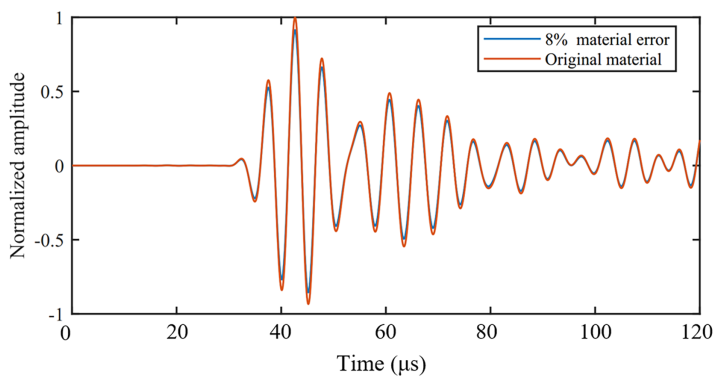

Figure 15: Effect of material property uncertainty on Lamb wave propagation.

As observed from the Lamb wave propagation waveforms in Fig. 15, material property uncertainty introduces small biases in TOF measurements. Although these deviations appear minor at the signal level and are not easily captured by conventional damage imaging methods, their influence is significantly amplified during FBP reconstruction. As shown in Fig. 14, even small TOF biases can lead to pronounced imaging artifacts, which substantially interfere with subsequent quantitative damage analysis.

Fig. 16 shows the TOF data recorded between transmitting sensor 1 and the remaining 63 receiving sensors under both the nominal material properties and the case with an 8% material deviation. Here, the horizontal axis denotes the sensing-path index, where indices 1 to 63 correspond sequentially to the propagation paths between sensor pair (1, 2) and sensor pair (1, 64). For most sensing paths, the overall TOF variation induced by material uncertainty remains relatively limited. However, for sensing paths that intersect or pass close to the damage region, particularly the path associated with sensor pair (1, 33), the material-induced TOF bias becomes significantly larger than that obtained under the nominal material parameters.

These localized TOF deviations are the primary cause of the pronounced reconstruction artifacts observed near the damage region in Fig. 14.

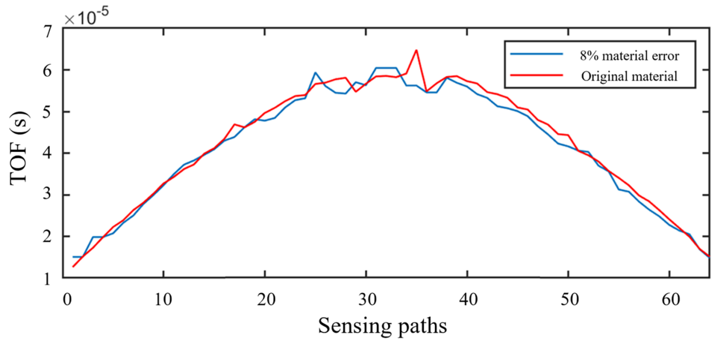

Figure 16: TOF changes in all the sensing paths due to different material properties.

For the nominal material properties, the TOF curves exhibit smooth and consistent trends, with noticeable deviations mainly restricted to sensing paths that intersect the damage region. In contrast, introducing an eight percent deviation in material properties leads to abnormal TOF fluctuations along several sensing paths, including sensor pairs 1 to 26, 1 to 29, and 1 to 30. These fluctuations result in nonlinear variations in the measured TOF. In addition, for the critical sensing path 1 to 33, which passes closest to the damage center, the TOF variation becomes less pronounced than that observed under nominal conditions. This inconsistency causes the reconstructed damage region to expand excessively and produces poorly defined boundaries, thereby reducing the clarity of the damage contour.

In practical structural health monitoring applications, accurate identification of damage characteristics, including location, centroid position, and geometric shape, is essential. To enable quantitative evaluation of these features, Canny edge detection [45] is applied to extract damage boundaries from the reconstructed images. To ensure a fair comparison, all compared methods were evaluated under the same Canny based edge extraction criterion and the same post processing setting, rather than under method specific threshold tuning.

To identify an appropriate filtering strategy for Lamb wave based FBP damage imaging and to achieve reliable edge extraction, several filtering methods are evaluated and compared prior to Canny edge detection. These methods include conventional Gaussian filtering [45], adaptive order statistic filtering (OSF) [46], smoothing filtering (SF) [47], convolutional smoothing filtering (CSF) [48], and the proposed dual scale morphological filtering (DSMF) approach [23]. The main characteristics and parameter settings of the filtering techniques used for comparison are summarized in Table 2, allowing a systematic assessment of their respective advantages and limitations.

Table 2: Parameter comparison of filtering methods for ultrasonic FBP images.

Method	Domain or Operations	Linear Characteristics	Element Type	Element Size
DSMF	Set operations	Non-linear	Structural element	$3 * 3$ and $5 * 5$
OSF	Spatial domain	Non-linear	Convolution element	$3 * 3$
SF	Spatial domain	Linear	Convolution element	$3 * 3$
CSF	Frequency domain	Linear	Convolution element	$3 * 3$
GF	Spatial domain	Linear	Convolution element	$3 * 3$ and $5 * 5$

It should be noted that the 3 × 3 and 5 × 5 structuring elements used in DSMF are relative image processing parameters defined on the fixed reconstruction grid, and are introduced for comparison under a common post processing setting rather than as directly calibrated physical dimensions.

DSMF differs fundamentally from conventional image filtering techniques in that it operates through set based morphological transformations rather than convolution in the time frequency domain. The structural elements used in DSMF are computationally simpler than convolution kernels and enable effective suppression of reconstruction artifacts while preserving the integrity of damage boundaries in ultrasonic FBP images of composite plates.

Conventional fault detection and control approaches, as well as most deep learning-based processing methods, have rarely addressed Lamb wave-based image filtering problems [49,50], and systematic investigations of filtering strategies specifically tailored for ultrasonic FBP images remain limited. Traditional filtering techniques exhibit inherent trade-offs. OSF is effective in suppressing non smooth random noise and generally produces fewer edge burrs than linear smoothing filters with kernels of comparable size. SF is mainly suited for attenuating low frequency noise and typically results in an overall smoothing of the image. CSF adjusts kernel size and properties to achieve moderate noise reduction. However, these conventional approaches struggle to simultaneously preserve the geometric contours of delamination defects in composite laminates and effectively suppress reconstruction artifacts.

In contrast, DSMF extracts structural information through topological interactions between the structural elements and the image, allowing noise suppression while maintaining edge continuity. When combined with Canny edge detection, the DSMF-Canny framework exploits geometric features to enhance edge extraction performance. By integrating large scale and small scale structural elements, DSMF-Canny achieves a balanced filtering strategy that suppresses noise while retaining fine boundary details, thereby improving the reliability of damage edge identification. The FBP reconstructed images processed using the different filtering methods are presented in Figs. 17 and 18 for comparison. The displayed results are binary edge maps, where black pixels denote detected edges with value 1 and white regions denote background with value 0.

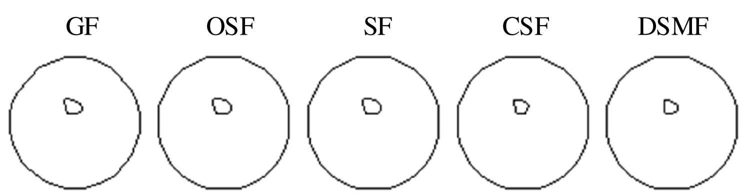

Figure 17: Edge detection results for each of the five methods (original material parameters).

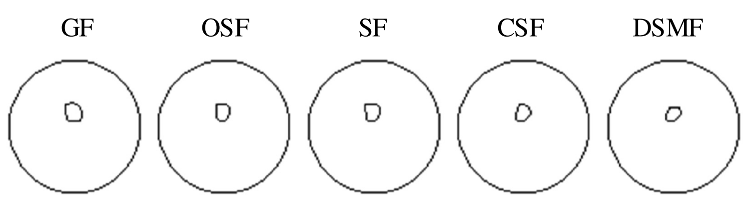

Figure 18: Edge detection results for each of the five methods (8% material error parameters).

A visual comparison of the edge detection results in Figs. 17 and 18 indicates that the boundaries extracted using the DSMF-Canny method exhibit the closest agreement with the predefined elliptical damage geometry. In contrast, the damage contours obtained using the other filtering approaches show noticeable outward deviations, leading to an overestimation of the damaged region. Such deviations directly affect the accuracy of subsequent damage area identification.

These observations demonstrate that the DSMF-Canny approach achieves superior accuracy in extracting damage boundaries from FBP-reconstructed images. The damage shapes obtained using DSMF-Canny are consistently closer to the reference ellipse defined in Fig. 14, not only under nominal material properties but also for FBP imaging results obtained in the presence of material property deviations arising from material uncertainty. This consistency highlights the robustness of the proposed DSMF–Canny framework against material-induced imaging artifacts.

Quantitative results for the extracted damage size, shape, and damage center coordinates are summarized in Tables 3 and 4.

Table 3: Numerical results of image edge detection by each of the five methods (original material parameters).

Image	Method	Set the Defect Center	Identified the Defect Center	Error	Set the Defect Area	Identified the Defect Area	Error (%)
Original material parameters FBP imaging	GF	(45, 55)	(46, 55)	(0, 0)	37.7	51.15	35.68
	OSF	(45, 55)	(46, 54)	(2, −1)	37.7	57.15	51.59
	SF	(45, 55)	(46, 55)	(−1, 1)	37.7	59.15	56.9
	CSF	(45, 55)	(44, 55)	(2, −2)	37.7	48.15	27.72
	DSMF	(45, 55)	(45, 55)	(0, 0)	37.7	44.15	17.11

Table 4: Numerical results of image edge detection by each of the five methods (8% material error parameters).

Image	Method	Set the Defect Center	Identified the Defect Center	Error	Set the Defect Area	Identified the Defect Area	Error (%)
Material parameters 8% error in FBP imaging	GF	(45, 55)	(46, 54)	(1, −1)	37.7	87.15	131.17
	OSF	(45, 55)	(46, 54)	(1, −1)	37.7	63.15	67.51
	SF	(45, 55)	(46, 54)	(1, −1)	37.7	70.15	86.07
	CSF	(45, 55)	(46, 53)	(1, −2)	37.7	61.15	62.2
	DSMF	(45, 55)	(45, 53)	(0, −2)	37.7	44.15	17.11

As summarized in Tables 3 and 4, when nominal material properties are adopted, the identification errors obtained using the other filtering methods are 35.68 percent, 51.59 percent, 56.9 percent, and 27.72 percent, respectively. In contrast, the proposed DSMF-Canny method achieves a substantially lower error of 17.11 percent. When an eight percent deviation in material parameters is introduced, the recognition errors associated with the conventional methods increase significantly, reaching 131.17 percent, 67.51 percent, 80.07 percent, and 62.2 percent, respectively. Notably, the identification error obtained using DSMF-Canny remains unchanged at 17.11 percent, demonstrating a clear advantage over the other approaches in terms of edge extraction accuracy under material uncertainty.

These results indicate that DSMF-Canny effectively enhances damage boundaries while suppressing spurious edges caused by reconstruction artifacts and material property variations. The consistent identification error observed under both nominal and perturbed material conditions confirms that DSMF exhibits a strong capability to mitigate errors induced by material uncertainty. For elliptical delamination with relatively complex geometry, the maximum deviation of the damage center location extracted using DSMF-Canny is limited to 2 mm, further highlighting the robustness of the proposed method.

Accordingly, the extracted boundary should be interpreted as the contour of the reconstructed damage indication after imaging and post processing, rather than as a strict one to one representation of the physical interface boundary.

Overall, the results demonstrate that DSMF-Canny significantly improves delamination detection accuracy in composite structures compared with conventional filtering and edge detection methods. Even in the presence of complex damage geometries and material property uncertainty, the proposed approach remains effective. When integrated with the filtered back projection imaging framework, DSMF-Canny substantially reduces edge distortion caused by reconstruction artifacts and material induced errors, enabling more accurate damage reconstruction and quantitative characterization of delamination in composite plates.

5 Conclusion

To address the limitations of conventional ultrasonic damage detection methods for accurately reconstructing delamination and quantifying its location and size in composite materials, this study evaluates damage imaging results from FBP combined with DSMF and Canny edge detection. Since the accuracy of FBP strongly depends on reliable TOF measurements, variations in material properties can introduce noticeable TOF errors, particularly along sensing paths that pass through damaged regions. To alleviate this issue, a CWT-based TOF measurement method is adopted. In addition, the influence of material uncertainty on the reconstructed imaging quality of stratified delamination damage is explicitly investigated. Because material uncertainties are difficult to quantify accurately through experiments, a point-force-based FE modeling approach is employed for systematic analysis.

The stability of FBP imaging under material uncertainty is examined using elliptical delamination with relatively complex geometry. Imaging cases are considered for both nominal T300 7901 material properties and scenarios with an 8% deviation in elastic properties. The results show that deviations in material properties significantly degrade the quality of FBP imaging. Since edge information plays a critical role in identifying delamination size, shape, and location, particular attention is paid to edge extraction performance. Comparisons between DSMF-Canny and other filtering methods applied to FBP images demonstrate that DSMF-Canny is more effective in compensating for errors caused by material property inaccuracies, especially in preserving edge features.

Quantitative analysis further confirms the effectiveness of the proposed DSMF-Canny and FBP framework. The damage area error is reduced from 35.68 percent to 17.11 percent under nominal material properties and from 131.17 percent to 17.11 percent when an eight percent material property deviation is introduced. Moreover, the maximum deviation of the estimated damage center coordinates obtained using DSMF-Canny is limited to 2 mm, indicating strong consistency with the predefined elliptical delamination. These results demonstrate that DSMF-Canny, combined with FBP imaging, can effectively compensate for the effects of material uncertainty on delamination reconstruction and edge information extraction.

It should be noted that the present results are obtained within a controlled numerical framework with idealized material perturbation and delamination modeling. Accordingly, the extracted TOF and boundary should be interpreted as imaging-oriented indicators rather than exact physical quantities. Future work may extend the framework to more complex structural configurations and damage scenarios.

Acknowledgement: Not applicable.

Funding Statement: This work was supported by the National Natural Science Foundation of China (No. 525B2079). In addition, the authors gratefully acknowledge the support from the China Association for Science and Technology Young Scientific and Technological Talent Cultivation Program and the ASA International Student Grant.

Author Contributions: Kai Luo contributed to writing–original draft, software, and methodology. Yuzhi Chen contributed to supervision and visualization. All authors reviewed and approved the final version of the manuscript.

Availability of Data and Materials: The authors state that they do not have the right to share the data.

Ethics Approval: Not applicable.

Conflicts of Interest: The authors declare no conflicts of interest.

References

1. Yu S, Luo K, Fan C, Fu K, Wu X, Chen Y, et al. Advancing spacecraft safety and longevity: a review of guided waves-based structural health monitoring. Reliab Eng Syst Saf. 2025;254(1):110586. doi:10.1016/j.ress.2024.110586.
2. Zhuang L, Luo K, Yang Z. A multimodal gated recurrent unit neural network model for damage assessment in CFRP composites based on Lamb waves and minimal sensing. IEEE Trans Instrum Meas. 2024;73:3506911–11. doi:10.1109/TIM.2023.3348884.
3. Jayakrishnan S, Suresh N, Koodalil D, Balasubramaniam K. Coded excitation for low-power guided ultrasonic wave inspection in safety-critical industries: case studies. Insight. 2021;63(12):712–20. doi:10.1784/insi.2021.63.12.712.
4. Capineri L, Bulletti A. Ultrasonic guided-waves sensors and integrated structural health monitoring systems for impact detection and localization: a review. Sensors. 2021;21(9):2929. doi:10.3390/s21092929.
5. Zhu K, Cao M, Kudela P, Ostachowicz W, Radzieński M. Effective thickness mapping for composite laminates based on full wavefield guided wave analysis. Mech Syst Signal Process. 2025;237:113068. doi:10.1016/j.ymssp.2025.113068.
6. Su C, Bian H, Jiang M, Zhang F, Sui Q. Research on composites damage identification based on power spectral density and Lamb wave tomography technology in strong noise environment. Compos Struct. 2022;289(2):115466. doi:10.1016/j.compstruct.2022.115466.
7. Alam P, Mamalis D, Robert C, Floreani C, Ó Brádaigh CM. The fatigue of carbon fibre reinforced plastics: a review. Compos Part B Eng. 2019;166(1):555–79. doi:10.1016/j.compositesb.2019.02.016.
8. Migot A, Saaudi A, Giurgiutiu V. Delamination depth detection in composite plates using the Lamb wave technique based on convolutional neural networks. Sensors. 2024;24(10):3118. doi:10.3390/s24103118.
9. Luo K, Ye L, Mustapha S, Chen Y, Yu S, Yang Z, et al. Baseline-free delamination detection in CFRP composites using guided wave-based virtual sensing paths. Ultrasonics. 2026;157(2):107772. doi:10.1016/j.ultras.2025.107772.
10. Cao X, Zeng L, Lin J, Hua J. Improving the resolution for Lamb wave testing via a smoothed Capon algorithm. Meas Sci Technol. 2018;29(4):045017. doi:10.1088/1361-6501/aaa7f9.
11. Zheng F, Yuan S. Guided Lamb wave array time-delay-based MUSIC algorithm for impact imaging. Sensors. 2024;24(6):1882. doi:10.3390/s24061882.
12. Nzouatchoua CB, Bentahar M, Montresor S, Colin N, Le Cam V, Trottier C, et al. Damage localization on composite structures based on the delay-and-sum algorithm using simulation and experimental methods. Sensors. 2023;23(9):4368. doi:10.3390/s23094368.
13. Luo K, Mustapha S, Chen Y, Ye L. Lamb wave-based improved virtual time-reversal method for damage detection of barely visible indentation damage in CF/EP sandwich composites. Compos Struct. 2026;377:119908. doi:10.1016/j.compstruct.2025.119908.
14. Guo J, Zeng X, Liu Q, Qing X. Lamb wave-based damage localization and quantification in composites using probabilistic imaging algorithm and statistical method. Sensors. 2022;22(13):4810. doi:10.3390/s22134810.

15. Lissenden CJ, Liu Y, Rose JL. Use of non-linear ultrasonic guided waves for early damage detection. Insight. 2015;57(4):206–11. doi:10.1784/insi.2015.57.4.206.
16. Chua CA, Alleyne DN, Calva M. Crack growth monitoring using low-frequency guided waves. Insight. 2017;59(2):64–71. doi:10.1784/insi.2017.59.2.64.
17. de Castro BA, Baptista FG, Alfredo Ardila-Rey J, Ciampa F. Baseline-free damage imaging algorithm using spatial frequency domain virtual time reversal. IEEE Trans Ind Inform. 2022;18(8):5043–54. doi:10.1109/TII.2021.3124924.
18. Tua PS, Quek ST, Wang Q. Detection of cracks in plates using piezo-actuated Lamb waves. Smart Mater Struct. 2004;13(4):643–660. doi:10.1088/0964-1726/13/4/002.
19. Wong ZZ, Chen S, Liu M, Lim SH, Cui F, Yao K. Piezoelectricity in structural adhesives and application for monitoring joint integrity via guided ultrasonic waves. IEEE Trans Ultrason Ferroelectr Freq Control. 2021;68(3):777–83. doi:10.1109/TUFFC.2020.3017760.
20. Cui R, Azuara G, Lanza di Scalea F, Barrera E. Damage imaging in skin-stringer composite aircraft panel by ultrasonic-guided waves using deep learning with convolutional neural network. Struct Health Monit. 2022;21(3):1123–38. doi:10.1177/14759217211023934.
21. Zhao X, Royer RL, Owens SE, Rose JL. Ultrasonic Lamb wave tomography in structural health monitoring. Smart Mater Struct. 2011;20(10):105002. doi:10.1088/0964-1726/20/10/105002.
22. Sha G, Soman R, Radzieński M, Cao M, Ostachowicz W, Zuo H. A two-step method for additional mass identification in beam structures by measurements of natural frequencies and guided waves. Measurement. 2021;186(4):110049. doi:10.1016/j.measurement.2021.110049.
23. Luo K, Chen L, Liang W, Weng H. A dual-scale morphological filtering method for composite damage identification using FBP. Mech Syst Signal Process. 2023;184:109683. doi:10.1016/j.ymssp.2022.109683.
24. Luo K, Chen L, Chen Y, Ye L, Yu S. An ultrasonic Lamb wave-based non-linear exponential RAPID method for delamination detection in composites. Compos Struct. 2025;352(14):118701. doi:10.1016/j.compstruct.2024.118701.
25. Wright W, Hutchins D, Jansen D, Schindel D. Air-coupled Lamb wave tomography. IEEE Trans Ultrason Ferroelectr Freq Control. 1997;44(1):53–9. doi:10.1109/58.585190.
26. Ridwan Effendi M, Anis Sekar Ningrum F, Amalia Amri N, Abubakar B, Risnanto S, Munir A. Interpolation effect on FBP-based image reconstruction of measured L-band microwave tomography. In: Proceedings of the 2021 IEEE International Conference on Communication, Networks and Satellite (COMNETSAT); 2021 Jul 17–18; Purwokerto, Indonesia. p. 290–3. doi:10.1109/comnetsat53002.2021.9530773.
27. Yan G. A Bayesian approach for damage localization in plate-like structures using Lamb waves. Smart Mater Struct. 2013;22(3):035012. doi:10.1088/0964-1726/22/3/035012.
28. Chen L, Xiao Q, Liang W, Hong J, Zou X. A time-of-flight revising approach to improve the image quality of Lamb wave tomography for the detection of defects in composite panels. Sci Eng Compos Mater. 2018;25(3):587–92. doi:10.1515/secm-2015-0399.
29. Li B, Liu Y, Gong K, Li Z. Damage localization in composite laminates based on a quantitative expression of anisotropic wavefront. Smart Mater Struct. 2013;22(6):065005. doi:10.1088/0964-1726/22/6/065005.
30. Abaqus/Explicit 6.12. [cited 2026 Jan 1]. Available from: http://www.3ds.com/products-services/simulia/.
31. Huber A. The dispersion calculator—a free software for calculating dispersion curves of guided waves. In: Proceedings of the 20th World Conference on Non-Destructive Testing (WCNDT 2024); 2024 May 27–31; Incheon, Republic of Korea. doi:10.58286/29894.
32. Nienwenhui JH, Neumann JJ, Greve DW, Oppenheim IJ. Generation and detection of guided waves using PZT wafer transducers. IEEE Trans Ultrason Ferroelectr Freq Control. 2005;52(11):2103–11. doi:10.1109/TUFFC.2005.1561681.
33. Liu YX, He AJ, Liu JH, Mao YW, Liu XZ. Location of micro-cracks in plates using time reversed nonlinear Lamb waves. Chin Phys B. 2020;29(5):311–7. doi:10.1088/1674-1056/ab81f7.
34. Wan X, Zhang Q, Xu G, Tse PW. Numerical simulation of nonlinear Lamb waves used in a thin plate for detecting buried micro-cracks. Sensors. 2014;14(5):8528–46. doi:10.3390/s140508528.

35. Barzegar M, Pasadas DJ, Ribeiro AL, Ramos HG, Lugovtsova Y, Bulling J. Polar coordinate for damage imaging of adhesively bonded plates using ultrasonic guided waves and laser Doppler vibrometer measurements. IEEE Trans Instrum Meas. 2023;72:6502611. doi:10.1109/TIM.2023.3267528.
36. Lang Y, Yang Z, Su Z, Wang Q, Chen X. A frequency diverse array (FDA) of dispersive Lamb waves for grating lobes suppression. Mech Syst Signal Process. 2025;241:113517. doi:10.1016/j.ymssp.2025.113517.
37. Luo K, Liu Y, Liang W, Chen L, Yang Z. Rapid damage reconstruction imaging of composite plates using non-contact air-coupled Lamb waves. NDT E Int. 2024;143(5):103047. doi:10.1016/j.ndteint.2024.103047.
38. Luo K, Chen L, Weng H, Li J, Liang W. Adaptive time-reversal method for delamination detection of composite plates based on reconstruction algorithm for probabilistic inspection of defects. Mech Syst Signal Process. 2023;196(5):110336. doi:10.1016/j.ymssp.2023.110336.
39. Liu M, Zhang W, Chen X, Li L, Wang K, Wang H, et al. Modelling guided waves in acoustoelastic and complex waveguides: from SAFE theory to an open-source tool. Ultrasonics. 2024;136(5):107144. doi:10.1016/j.ultras.2023.107144.
40. Huber AMA. Classification of solutions for guided waves in fluid-loaded viscoelastic composites with large numbers of layers. J Acoust Soc Am. 2023;154(2):1073–94. doi:10.1121/10.0020584.
41. Galán-Pinilla CA, E-Quiroga J, Peña-Ballesteros DY, Acosta-Minoli CA, González-Estrada OA. Comparative study of dispersion curves for LAMB waves using analytical solutions and semi-analytical methods. Appl Sci. 2023;13(3):1706. doi:10.3390/app13031706.
42. Duan W, Gan TH. Investigation of guided wave properties of anisotropic composite laminates using a semi-analytical finite element method. Compos Part B Eng. 2019;173(4):106898. doi:10.1016/j.compositesb.2019.106898.
43. Wang A, Li R, Liu X. Analysis of the tensile properties and probabilistic characteristics of large-tow carbon fiber-reinforced polymer composites. Polymers. 2024;16(15):2197. doi:10.3390/polym16152197.
44. Yang G, Xiao S, Hou C, Wan X, Gong J, Xia D. Multiscale uncertainty quantification of woven composite structures by dual-correlation sampling for stochastic mechanical behavior. Polymers. 2025;17(19):2648. doi:10.3390/polym17192648.
45. Canny J. A computational approach to edge detection. IEEE Trans Pattern Anal Mach Intell. 1986;8(6):679–98. doi:10.1109/tpami.1986.4767851.
46. Pitas I, Venetsanopoulos AN. Order statistics in digital image processing. Proc IEEE. 1992;80(12):1893–921. doi:10.1109/5.192071.
47. George G, Oommen RM, Shelly S, Philipose SS, Varghese AM. A survey on various Median filtering techniques for removal of impulse noise from digital image. In: Proceedings of the 2018 Conference on Emerging Devices and Smart Systems (ICEDSS); 2018 Mar 2–3; Tiruchengode, India. p. 235–8. doi:10.1109/ICEDSS.2018.8544273.
48. Sealy G, Wyvill G. Smoothing of three dimensional models by convolution. In: Proceedings of the 1996 Conference on Computer Graphics International. Washington, DC, USA: IEEE; 1996. p. 184–90.
49. Ruan Y, Yang Z, Lang Y, He D, Lu M, Chen X. Point-to-point dispersion estimation of Lamb waves. J Nondestruct Eval. 2025;44(2):61. doi:10.1007/s10921-025-01200-1.
50. Marzani A, Testoni N, De Marchi L, Messina M, Monaco E, Apicella A. An open database for benchmarking guided waves structural health monitoring algorithms on a composite full-scale outer wing demonstrator. Struct Health Monit. 2020;19(5):1524–41. doi:10.1177/1475921719889029.